Enhancement of thermoelectric power factor by inducing octahedral ordering in La$_{2-x}$Sr$_x$CoFeO$_6$ double perovskites

Khagesh Tanwar,[1,5,*] Deepankar Sri Gyan,[1,2,*] Shovit Bhattacharya,[3] Satish Vitta,[4] Akansha Dwivedi,[2] and Tanmoy Maiti[1,5,†]

[1]*Plasmonics and Perovskites laboratory, Indian Institute of Technology, Kanpur, UP 208016, India*
[2]*Department of Ceramic Engineering, Indian Institute of Technology (BHU) Varanasi 221005, India*
[3]*Technical Physics Division, Bhabha Atomic Research Center, Mumbai 400 085, India*
[4]*Department of Metallurgical Engineering and Materials Science, Indian Institute of Technology Bombay, Mumbai 400 076, India*
[5]*Department of Materials Science and Engineering, Indian Institute of Technology, Kanpur, UP 208016, India*

Among the various oxide thermoelectric materials, double perovskites provide more flexibility to maneuver interdependent thermoelectric parameters to achieve enhanced thermoelectric figure of merit (ZT), as octahedral ordering, i.e., arrangement of $B'O_6$ and $B''O_6$ octahedra, present in the $A_2B'B''O_6$ structure is impacted by cation doping. In this work, we investigated the role of octahedral distortion on thermoelectric properties of La$_{2-x}$Sr$_x$CoFeO$_6$ (LSCF) double perovskites with $0.0 \leqslant x \leqslant 1.0$, synthesized by the autocombustion route. Rietveld refinement of x-ray diffraction data revealed the phase transition with increasing Sr concentration (x) in LSCF from rhombohedral crystal structure with R-$3c$ space group ($x \leqslant 0.6$) to monoclinic $P2_1/n$ ($0.8 \leqslant x \leqslant 1.0$) space group. X-ray photoemission spectroscopy analysis further confirmed the presence of multiple oxidation states of Co and Fe, and shifts in oxidation states population driven by Sr content. These multivalent cations participated in the charge transport mechanism, which was explained by the small polaron hopping conduction model in these double perovskites. The electrical conductivity at room temperature was found to be increased by more than 10^7 times in LSCF due to Sr doping, causing a large enhancement in the thermoelectric power factor. Gradual decrease in the octahedral tilt angle with increasing Sr content in LSCF, leading toward the change of crystal structure from disordered (R-$3c$) to rock-salt-ordered ($P2_1/n$) double perovskites, was found to be responsible for the large decrease in activation energy barrier for small polaron hopping conduction in the LSCF system, resulting in the phenomenal increase in electrical conductivity. Maximum thermoelectric figure of merit, ZT = 0.11 was obtained at 723 K for La$_{2-x}$Sr$_x$CoFeO$_6$ with $x = 0.2$ composition.

I. INTRODUCTION

The thermoelectric (TE) power generator, as a potential alternative to renewable energy generation by utilizing waste heat, has attracted the attention of researchers in the recent years [1]. The energy conversion efficiency of a TE material is given by a dimensionless figure of merit, defined as $ZT = \frac{S^2\sigma}{\kappa}T$, where, ($\sigma$) electrical conductivity, (S) thermopower or Seebeck coefficient, and (κ) thermal conductivity [2–5]. In the past few decades, studies on chalcogenide-based systems such as Bi$_2$Te$_3$ [6,7], PbTe [8], etc. showed a good thermoelectric figure of merit (ZT). However, their toxicity, instability at high temperature, high processing cost, and environmental concerns curbed the realization of large-scale commercialization. This shifted the attention of researchers towards oxide materials, which promised high thermal stability, least environmental damage, and relatively much easier and economical synthesis [9]. Although many oxide materials such as ZnO [10], CaMnO$_3$ [11], NaCo$_2$O$_4$ [12], Ca$_3$CoO$_6$ [13], SrTiO$_3$ [9], etc. showed potential to be used in TE generators, their ZT values are much lower than those of intermetallics and

chalcogenides. Hence, engineering new oxide materials is of utter importance.

Recently, double perovskite materials $(A'A''B'B''O_6)$, where A'/A'' (A site) = La, Sr, Ba, etc. and B'/B'' (B site) = Fe, Co, Mn, Mo, Ti, etc. were studied for thermoelectric applications, and they exhibited a reasonably high power factor ($S^2\sigma$), which is considered as a primary governing factor for thermoelectric power generation efficiency [14–17]. However, double perovskites have been studied extensively for their structural, electronic, and magnetic properties [18–22] since 1950's. Charge carrier transport and magnetic properties of these double perovskites were largely characterized by octahedral ordering in structure and spin states of B-site cations. In 1993, Anderson *et al.* [23] suggested that the favored arrangement of $B'O_6$ and $B''O_6$ octahedra depends either on charge differences or ionic size differences of B-site cations. For instance, the ordered state is typically favored when the charge difference of B-site cations is two or more; otherwise, a random arrangement of $B'O_6$ or $B''O_6$ octahedra is dominant. Similarly, based on the ionic size difference a random arrangement (less than 0.01 Å), a rock-salt-ordered state (0.01−0.08 Å) or layered ordered (0.08−0.12 Å) arrangement of $B'O_6$ or $B''O_6$ octahedra is observed.

To engineer suitable thermoelectric materials, it is essential to optimize the thermoelectric performance by optimizing

*These authors contributed equally to this work.
†Corresponding author: tmaiti@iitk.ac.in

electrical conductivity, thermal conductivity, and the See-beck coefficient. However, in general, it is intractable since the electrical conductivity follows an opposite trend of the Seebeck coefficient with respect to carrier concentration and effective mass of charge carrier. Additionally, the thermal conductivity, a contribution of lattice and electronic thermal conductivity, should be as low as possible [24]. A decrease in lattice thermal conductivity can be accomplished by intro-ducing nano grain size, lattice defects, and chemical inho-mogeneities [17,25]. Fortunately, in these double perovskite based oxides with multivalent cations, a plethora of defects are introduced during materials synthesis, which act as phonon scattering centers rendering enhanced thermoelectric perfor-mance [15,26]. In the present investigation, efforts were made to optimize the thermoelectric performance of La_2CoFeO_6 (LCF) double perovskites by substituting Sr^{2+} at the La^{3+} site. LCF and its doping variants were previously studied for magnetic, electronic, and structural properties [20,27,28]. However, no such reports on thermoelectric properties of LCF was found in the literature simply because LCF is an insulator in nature, and its highly localized charge carriers are very discouraging for thermoelectric application. Here we have shown that the activation energy barrier of charge carriers governed by small polaron hopping can be lowered by 12 times and fractional polaron concentration can be increased by 14 times in LCF by Sr substitution in such a way so that octahedral arrangement in the perovskite structure becomes more ordered, resulting in more than a 10^7 times increase in electrical conductivity.

A series of compositions in the double perovskite system $La_{2-x}Sr_xCoFeO_6$ ($x = 0.0$, 0.1, 0.2, 0.4, 0.6, 0.8, and 1.0) (LSCF) were synthesized by the citrate-nitrate autocombus-tion route to examine structural, microstructural, and ther-moelectric behaviors. Structural transition with increasing Sr concentration was studied using Rietveld refinement of powder x-ray diffraction (XRD) data. The potential of these LSFC double perovskites for thermoelectric applications were further evaluated by measuring electrical conductivity, See-beck coefficient, and thermal conductivity. The conduction mechanism of these oxides was explained by the small po-laron hopping model, defect chemistry, and a modified Heikes formula. The immense increase in electrical conductivity was triggered by enhancement of octahedral ordering with the virtue of reducing local fields on increasing Sr content in LCF, as if the localized charge carriers started behaving like itiner-ant state. Subsequently, this increase in electrical conductivity played a vital role in enhancing the ZT of Sr-doped LFC, which otherwise behaved as an insulating material.

II. EXPERIMENTAL

$La_{2-x}Sr_xCoFeO_6$ ($x = 0.0$, 0.1, 0.2, 0.4, 0.6, 0.8, and 1.0) (LSCF) double perovskite nanopowders were synthesized using the citrate-nitrate autocombustion route. Compositions were abbreviated as LSCF00 ($x = 0.0$), LSCF02 ($x = 0.2$), LSCF04 ($x = 0.4$), LSCF06 ($x = 0.6$), LSCF08 (0.8) and LSCF10 ($x = 1.0$). La_2O_3 (Sigma Aldrich, >99%), $SrCO_3$ (Sigma Aldrich, >99%), $Fe(NO_3)_3 \cdot 6H_2O$ (Fisher Scientific, >97%), and Co_3O_4 (Sigma Aldrich, >99%) were used as raw materials. A stoichiometric amount of Lanthanum oxide,
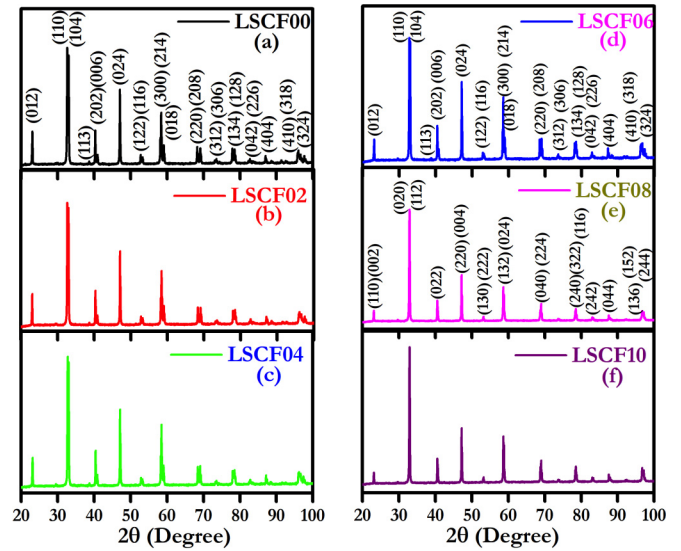
FIG. 1. Powder x-ray diffraction patterns of (a) LSCF00, (b) LSCF02, (c) LSCF04, (d) LSCF06, (e) LSCF08, and (f) LSCF10.

Strontium carbonate, and Cobalt oxide were mixed separately in dilute Nitric acid followed by heating at 373, 383, and 403 K, respectively, to obtain $La(NO_3)_3$, $Sr(NO_3)_2$, and $Co(NO_3)_3$. Nitrates were mixed into a solution of citric acid keeping the citrate to nitrate ratio (C:N) ~ 0.3 for smooth combustion [29]. The mixture was stirred continuously at 473 K to obtain a viscous solution that then underwent gela-tion followed by foaming and autoignition resulting into ashes after complete combustion. The ash obtained was ground in an agate mortar pestle and calcined at 1073 K for 6 h to obtain single phase solid solution of LSCF double perovskites. The powder was mixed with 2% PVA solution and pressed to obtain cylindrical pellets of $\sim 15\,mm \times \sim 2\,mm$ dimensions. The binder burnout for the pellets was carried out at 873 K for 2 h followed by sintering at 1573 K for 10 h. Powder x-ray diffraction patterns for all the LSCF compositions were recorded using a Rigaku Smartlab x-ray diffractometer in the 2θ range 10–110°. For the microstructural investigation, pol-ishing of the sintered pellets was done followed by gold coat-ing to make the surface conducting. Field emission scanning electron microscope (FE-SEM) micrographs were collected using NOVA NANOSEM 450 machine. X-ray photoemission spectroscopy (XPS) spectra were recorded using PHI 5000 Versaprobe II. Electrical conductivity and Seebeck coefficient were measured in temperature range 300–1123 K using ZEM-3M10 apparatus (ULVAC-RIKO Inc.), and power factor was calculated. Thermal diffusivity was measured for selected compositions by using LFA 457 NETZSCH. Specific heat was measured using Netzsch DSC 204 f1 instrument.

III. STRUCTURAL AND MICROSTRUCTURAL ANALYSIS

As depicted in Fig 1, powder XRD patterns affirm the formation of single-phase solid solution in all the synthesized compositions. XRD profiles were indexed with the *R-3c* space group (disordered double perovskite structure) for the LSCF compositions $0.0 \leqslant x \leqslant 0.6$. La_2CoFeO_6 (LSCF00, $x = 0.0$) [20,27] was previously reported to exhibit rhombohedral
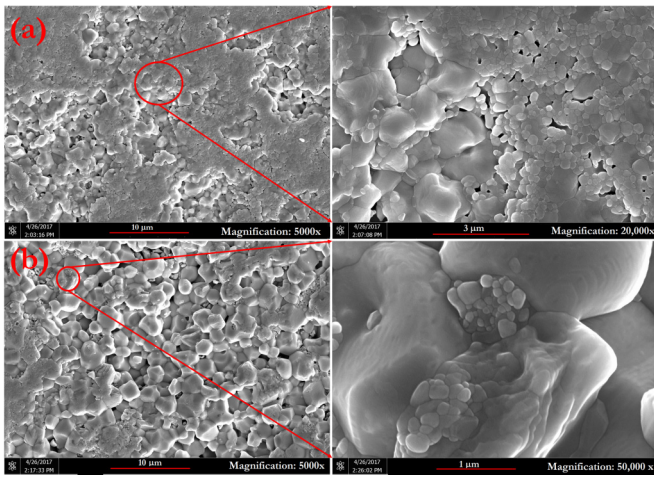
FIG. 2. FE-SEM micrographs for (a) LSFC02 and (b) LSFC04; side panel shows magnified view for better visualization.

crystal structure with the *R-3c* space group, which is consistent with the present investigation, until $x = 0.6$. On further increasing the Sr concentration, the crystal structure changes to monoclinic with the $P2_1/n$ space group, which is evident from the XRD profiles of compositions $x = 0.8$ and 1.0, indexed with respect to the $P2_1/n$ space group (rock-salt-ordered double perovskite structure), as shown in Figs. 1(e) and 1(f). The composition with $x = 1.0$ (LaSrCoFeO$_6$) was previously investigated by using neutron diffraction and reported to exhibit monoclinic crystal structure with the $P2_1/n$ space group [30].

However, it is essential to pinpoint the parameters responsible for structural change to optimize their thermoelectric properties. In the present report, we have carried out a detailed investigation on the change in crystal symmetry with increasing Sr concentration, as explained in Sec. VI.

Microstructure plays a vital role in defining thermoelectric properties. In optimizing thermoelectric performance, it is essential to decrease thermal conductivity without compromising electrical conductivity. Since electronic thermal conductivity is directly proportional to electrical conductivity, reduction of lattice thermal conductivity is preferred [31].

One way to decrease lattice thermal conductivity is by increasing the interfaces via reducing grain size. In the present study, FE-SEM was employed to study the microstructure of the prepared compositions. Figure 2 depicts the FE-SEM images of the fractured surface of two selected compositions, LSCF02 and LSCF04. All the samples exhibited dense microstructure. The microstructure of these double perovskites was found to be a combination of nm-scale smaller grains with μm-scale larger grains. However, the concentration of smaller grains decreased with increasing Sr content and with larger grains grew bigger. It suggests that incorporation of Sr in LFC facilitates the grain growth of these oxides.

IV. XPS Spectra

In these complex double perovskites, *B*-site cations often represent multiple oxidation states for charge compensation in the structure [18]. In the present case, substitution of Sr^{2+} in place of La^{3+} would create charge imbalance in the structure,

which is expected to be neutralized by change in the oxidation states of multivalent *B*-site cations (Fe or Co). To identify the oxidation states of *B*-site cations, XPS spectra were recorded for the samples LSCF00 and LSCF10. High resolution XPS spectra of the Co 2*p* and Fe 2*p* for the compositions LSCF00 and LSCF10 are depicted in Fig. 3. The XPS peaks were deconvoluted into Lorentzian-Gaussian peaks after background correction. The binding energy and oxidation states were estimated in comparison with adventitious carbon of binding energy 284.55 eV [32]. The binding energy and area under the XPS peaks corresponding with all the cations are enlisted in Table I. Binding energies of all the oxidation states were found to be similar to what was reported in the literature [33–36].

It is evident from the XPS analysis that Fe and Co were present in the multiple oxidation states in these perovskites. In the composition LSCF00, Co exhibited +2 and +3 oxidation states, while Fe showed +2, +3, and +4 oxidation states. On the other hand, in the composition LSCF10, Co was present as +2 and +3 oxidation states, while Fe was present in only +3 and +4 oxidation states. It is important to notice that the ratio of Co^{3+} and Co^{2+} changed from 1:1 in LSCF00 to 3:2 in LSCF10. It implies that due to incorporation of Sr^{2+} in place of La^{3+} in the LSCF system, the majority of Co preferred to possess a +3 oxidation state compared to +2. Similarly, the existence of iron as Fe^{4+} state was found to be increased from ∼28%, in LSCF00 to ∼50% in LSCF10, while in the case of the Fe^{3+} state it decreased from ∼53% to ∼50%. Additionally, in LSCF00, ∼18% of Fe possessed a +2 oxidation state, while in LSCF10, Fe^{2+} was found to be absent. It clearly signifies that with increasing Sr content, the oxidation states of Fe and Co increased to favor the charge neutrality of the system.

V. THERMOELECTRIC ANALYSIS

In order to evaluate the thermoelectric behavior of LSCF double perovskites, the Seebeck coefficient and electrical conductivity were measured in the temperature range of 300–1123 K, and power factors ($S^2\sigma$) were calculated for all the compositions. Variation of the Seebeck coefficient (S), electrical conductivity (σ), and power factor ($S^2\sigma$) with temperature is shown in Fig. 4 (left column). At 323 K, the electrical conductivity of LSCF00 was found to be 7.2×10^{-3} S/m, suggesting it to be electrically insulating in nature. On the other hand, at 323 K the electrical conductivity in LSCF10 was found to be 1.42×10^5 S/m, which is 10^7 times higher than that of LSCF00. This spectacular increase in electrical conductivity is an effect of Sr doping. As temperature rose, in LSCF00, the conductivity gradually increased, attaining 5.1×10^3 S/m, suggesting semiconductor-like behavior. With increasing temperature, LSCF00 and LSCF02 showed semiconductor-like behavior in the investigated temperature range, while in the compositions $x \geqslant 0.4$, semiconductor ($d\sigma/dT > 0$) to metal-like ($d\sigma/dT < 0$) transition was observed above 673 K. This transition temperature (T_{S-M}) showed a decreasing trend with increasing Sr concentration. The Seebeck coefficient was found to be positive in all the compositions throughout the measurement range, which suggests *p*-type semiconductor-like behavior in all the
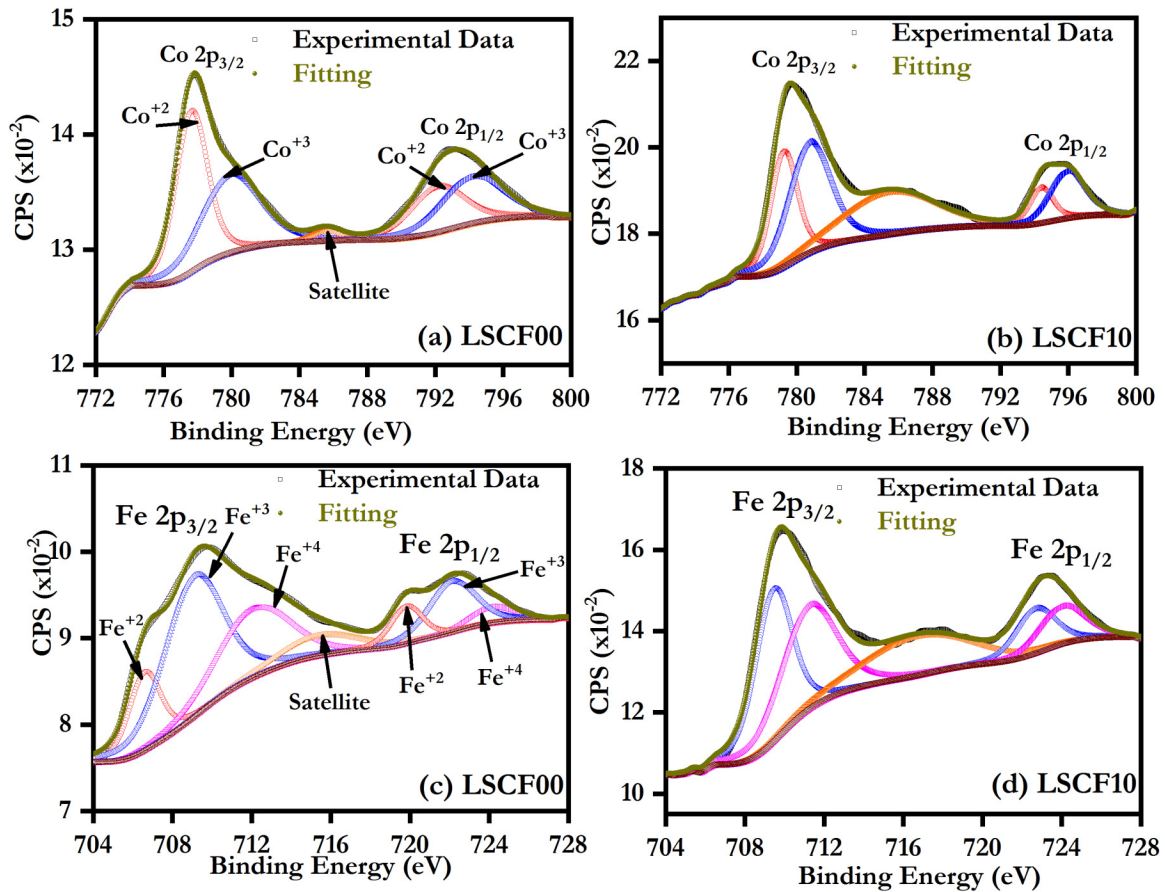
FIG. 3. XPS spectra for (a) LSCF00 Co 2*p*, (b) LSCF10 Co 2*p* (c) LSCF00 Fe 2*p*, and (d) LSCF10 Fe 2*p*.

TABLE I. Binding energy and percentage area obtained by deconvolution of XPS spectra for different oxidation states of iron and cobalt

Composition	Oxidation state	Binding Energy (eV)	Area (%)
LSCF00	Co^{3+} $2p_{3/2}$	779.92	49.76
	Co^{3+} $2p_{1/2}$	794.14	
LSCF10	Co^{3+} $2p_{3/2}$	780.78	61.55
	Co^{3+} $2p_{1/2}$	795.96	
LSCF00	Co^{2+} $2p_{3/2}$	777.64	50.24
	Co^{2+} $2p_{1/2}$	792.15	
LSCF10	Co^{2+} $2p_{3/2}$	779.26	38.45
	Co^{2+} $2p_{1/2}$	794.42	
LSCF00	Fe^{4+} $2p_{3/2}$	712.10	28.25
	Fe^{4+} $2p_{1/2}$	724.07	
LSCF10	Fe^{4+} $2p_{3/2}$	711.23	50.16
	Fe^{4+} $2p_{1/2}$	723.99	
LSCF00	Fe^{3+} $2p_{3/2}$	709.08	53.30
	Fe^{3+} $2p_{1/2}$	722.15	
LSCF10	Fe^{3+} $2p_{3/2}$	709.46	49.84
	Fe^{3+} $2p_{1/2}$	722.69	
LSCF00	Fe^{2+} $2p_{3/2}$	706.60	18.45
	Fe^{2+} $2p_{1/2}$	719.83	
LSCF10	Fe^{2+} $2p_{3/2}$	–	–
	Fe^{2+} $2p_{1/2}$	–	

compositions. The maximum value of the Seebeck coefficient, 287 μV/K, was obtained in the composition LSCF00 at 323 K, which decreased with increasing Sr concentration as expected from the large increase in electrical conductivity observed in these oxides. Thermopower showed a decreasing trend with increasing temperature with a slight increment after semiconductor-to-metal-like transition temperature. The power factor was calculated combining both the effect of electrical conductivity and the Seebeck coefficient as depicted in Fig. 4. The maximum power factor, 222 μW/mK^2, was obtained in the LSCF02 composition. On further increasing Sr concentration ($x > 0.2$), the power factor showed a decreasing trend since the S value decreased, although σ increased. The power factor of LSCF00 was found to be very low due to low electrical conductivity.

After analyzing the power factor behavior, LSCF02 and LSCF04 compositions were selected for further investigation of thermal conductivity in order to evaluate the thermoelectric figure of merit, ZT. Thermal conductivity was calculated using the formula, $\kappa = \rho C_P D$; where, D is thermal diffusivity, C_P is heat capacity and ρ is the density of the sample. Thermal diffusivity was measured in the temperature range of 300–873K. Figure 4 (right column) shows the behavior of total thermal conductivity, lattice thermal conductivity, electronic thermal conductivity, and calculated ZT values for LSCF02 and LSCF04 compositions. At 323 K, thermal conductivities of LSCF02 and LSCF04 were found to be 1.36 and 1.55 W/mK, respectively. With increasing temperature, there was
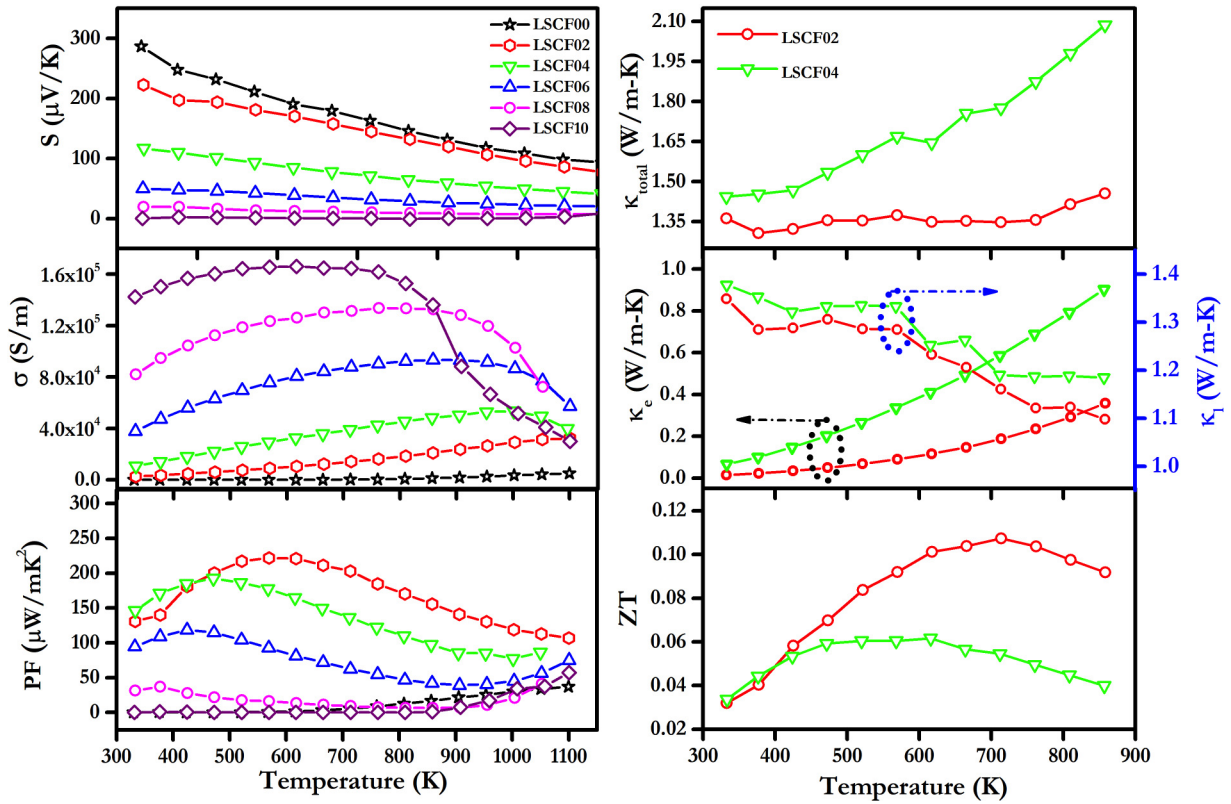
FIG. 4. (Left column) Seebeck coefficient (S), Electrical conductivity (σ), and power factor ($S^2\sigma$) for all the LSCF compositions; (right column) total thermal conductivity (κ_{total}), lattice (κ_l) and electronic (κ_e) thermal conductivity, and ZT for LSCF02 and LSCF04 compositions.

almost no variation in thermal conductivities of LSCF02 exhibiting maximum thermal conductivity of 1.45 W/mK at 858.5 K. On the other hand, thermal conductivity of LSCF04 increased gradually with temperature reaching a maximum of 2.08 W/mK at 858.5 K. The electronic thermal conductivity (κ_e) was calculated using the Wiedemann-Franz law, $\kappa_e = LT\sigma$; where, L is the Lorentz number, T is temperature in Kelvin, and σ is the electrical conductivity. The Lorentz number was calculated by using the formula [37] $L = 1.5 + e^{[-\frac{S}{116}]}$. The lattice thermal conductivity ($\kappa_l = \kappa_{\text{total}} - \kappa_e$) decreased almost linearly with increasing temperature, suggesting the dominance of Umklapp scattering [38]. Since the lattice thermal conductivity remained almost the same for these two compositions, higher thermal conductivity (κ_{total}) obtained for LSCF04 composition is due to higher κ_e values as compared to LSCF02. Moreover, the increasing trend observed in the κ vs T graph in LSCF04 samples originates from the increasing trend of κ_e with temperature. However, the thermal conductivity values obtained in these double perovskites are much lower than what was reported for other similar perovskite-based oxides [39]. Furthermore, the thermoelectric figure of merit, ZT, was calculated for LSCF02 and LSCF04 compositions. A maximum ZT value of 0.11 was obtained at 723 K in LSCF02 composition.

VI. RIETVELD REFINEMENT AND STRUCTURE CORRELATION WITH ELECTRICAL CONDUCTIVITY

It is evident from the thermoelectric analysis that the orders of magnitude increase in electrical conductivity of pure LFC

by Sr-doping played the crucial role in attaining an enhanced thermoelectric power factor and ZT in the LSCF system. In order to unravel the role of the crystal structure and octahedral ordering on the colossal increase in electrical conductivity, Rietveld refinement was carried out on XRD data using the FullProf Program [40] to analyze the parameters responsible for the crystal symmetry change that occurred with increasing Sr content. Based on previous reports, we performed the Rietveld refinement using R-$3c$ and $P2_1/n$ space groups for all the compositions. However, refinement results fit better for R-$3c$ up to $x = 0.6$ composition and $P2_1/n$ for $x = 0.8$ and 1.0 compositions. Rietveld refinement patterns of the LSFC00 and LSFC08 compositions along with their schematic diagrams of unit cells are depicted in Fig. 5. During the refinement, the peak shapes were described by the Pseudo-Voigt function, while the background was described by linear interpolation between a set of selected background points. In the final run, scale factor, zero correction, lattice parameters, atomic positions, asymmetry parameters, and thermal parameters were refined simultaneously. Appreciably low values of the R factor such as R_p, R_{wp}, R_{exp}, R_B, and χ^2, as presented in Table II, ensured satisfactory fitting. All the compositions produced good fitting.

Table III presents important bond lengths, bond angles, and unit cell parameters evaluated after Rietveld refinement for all the compositions. The Fe/Co–O bond length showed a decreasing trend with increasing dopant concentration, while the R-$3c$ symmetry is maintained. On the other hand, the O–Fe/Co–O bond angle increases in one direction while decreases in another direction in the compositions with $x = 0.8$
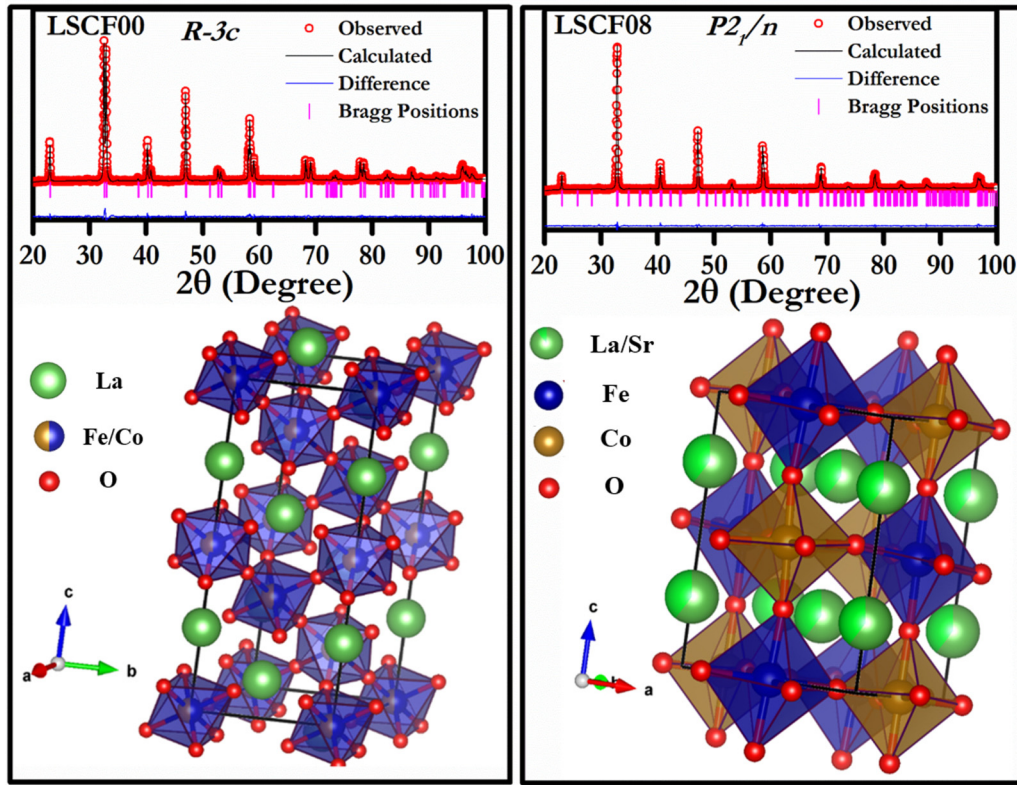
FIG. 5. Rietveld refinement plots for LSCF00 and LSCF08 compositions with corresponding schematic structure.

and 1.0. Furthermore, as depicted in Fig. 6(a), the lattice parameters $a = b$ and c decreases continuously up to $x = 0.6$. In Fig. 6(a), to compare the lattice parameters we have plotted a and c_{eq} (calculated by $18c_{eq}^2 = c_H^2 + 12a_H^2$; where c_H and a_H are lattice parameters of the rhombohedral phase in a hexagonal setting) in compositions up to $x = 0.6$, but a, b, and $c/\sqrt{2}$ in compositions $x = 0.8$ and 1.0 [41–43]. The lattice parameters of LSCF08 and LSCF10 compositions were found to be lower than that of the *R-3c* phases of $0 \leqslant x \leqslant 0.6$ compositions, although they remained almost similar for the LSCF08 and LSCF10 compositions. The decrease in lattice parameters in spite of doping with larger ion Sr^{2+} doping can

be explained by the increased concentration of smaller ions (Fe^{4+} and Co^{3+}) on the *B*-site, as verified by the XPS analysis. However, to precisely apprehend the impact of Sr doping, it is crucial to consider distortions in octahedra due to octahedral tilting. The average tilt angle (φ) was calculated for all the compositions using the following equations [43]:

$$\cos\theta_1 = \frac{2 - 5\cos^2\varphi_1}{2 + \cos^2\varphi_1}, \qquad (1)$$

$$\cos\theta_2 = \frac{1 - 4\cos^2\varphi_2}{3}, \qquad (2)$$

TABLE II. Refined structural parameters, unit cell parameters, and reliable factors by the Rietveld method for LSCF00 and LSCF08 compositions.

Composition	Space Group	Cell parameters	Atoms	Atomic Positions			B_{iso}	Reliable Factors
				x	y	z		
LSCF00	*R-3c*		La	0.0000	0.0000	0.2500	0.03	$R_p = 16.50$
		$a = 5.4935\,\text{Å}$	Co	0.0000	0.0000	0.0000	0.21	$R_{wp} = 11.00$
		$c = 13.2357\,\text{Å}$	Fe	0.0000	0.0000	0.0000	0.21	$R_{exp} = 8.67$
			O	0.5482	0.0000	0.2500	0.31	$R_B = 2.48$
								$\chi^2 = 1.61$
LSCF08	*P2$_1$/n*		La	0.4976	0.4985	0.2457	0.05	
		$a = 5.4403\,\text{Å}$	Sr	0.4976	0.4985	0.2457	0.05	$R_p = 18.30$
		$b = 5.4618\,\text{Å}$	Fe	0.0000	0.5000	0.0000	0.30	$R_{wp} = 10.10$
		$c = 7.7041\,\text{Å}$	Co	0.5000	0.0000	0.0000	0.62	$R_{exp} = 8.57$
			O1	0.2486	0.2306	0.0223	0.86	$R_B = 1.92$
		$\beta = 90.207°$	O2	0.2305	0.7603	0.0008	0.37	$\chi^2 = 1.39$
			O3	0.5106	0.0297	0.2606	0.13	

TABLE III. Unit cell parameters, Bond lengths, and Bond angles for all the compositions

Composition	Space group	Cell parameters	Bond Lengths (Å)	Bond Angles (°)
LSCF00	R-3c	$a = 5.4935$ Å $c = 13.2357$ Å	Fe/Co–O = 1.949	O–Fe/Co–O = 91.14, 88.86
LSCF02	R-3c	$a = 5.4905$ Å $c = 13.2580$ Å	Fe/Co–O = 1.948	O–Fe/Co–O = 91.00, 88.99
LSCF04	R-3c	$a = 5.4856$ Å $c = 13.2733$ Å	Fe/Co–O = 1.944	O–Fe/Co–O = 90.84, 89.16
LSCF06	R-3c	$a = 5.4785$ Å $c = 13.2864$ Å	Fe/Co–O = 1.939	O–Fe/Co–O = 90.64, 89.35
LSCF08	$P2_1/n$	$a = 5.4403$ Å $b = 5.4618$ Å $c = 7.7041$ Å $\beta = 90.207°$	Fe–O1 = 2.005 Fe–O2 = 1.895 Fe–O3 = 1.852 Co–O1 = 1.965 Co–O2 = 1.867 Co–O3 = 2.014	O1–Fe–O2 = 84.02, 95.98 O1–Fe–O3 = 89.86, 90.14 O2–Fe–O3 = 87.37, 92.63 O1–Co–O2 = 84.39, 95.60 O1–Co–O3 = 82.67, 97.33 O2–Co–O3 = 86.02, 93.98
LSCF10	$P2_1/n$	$a = 5.4427$ Å $b = 5.4547$ Å $c = 7.7089$ Å $\beta = 90.207°$	Fe–O1 = 1.928 Fe–O2 = 1.950 Fe–O3 = 1.903 Co–O1 = 1.920 Co–O2 = 1.945 Co–O3 = 1.959	O1–Fe–O2 = 87.62, 92.38 O1–Fe–O3 = 84.88, 95.12 O2–Fe–O3 = 81.98, 98.03 O1–Co–O2 = 88.56, 91.44 O1–Co–O3 = 79.34, 100.66 O2–Co–O3 = 86.96, 93.04

where, θ_1 and θ_2 are Fe/Co-O-Fe/Co angles, while φ (avg. of φ_1 and φ_2) is the tilt angle along [111] pseudocubic directions. Figure 6(b) shows the variation of average tilt angle (φ) with varying Sr concentration. Interestingly, the average tilt angle decreases with increasing Sr concentration, which explains the change of crystal structure from disordered (R-3c) to rock-salt-ordered ($P2_1/n$) double perovskites. Furthermore, the manifold enhancement in electrical conductivity is also an outcome of decreased distortion in the structure. Since, the presence of distortions induces variation in local fields, it renders the localization of charge carriers, resulting in a large activation energy barrier for charge transport, which reduces significantly when the structure becomes ordered. However, in the present investigation the enhancement in conductivity is a combined effect of decreased distortions and increase in total number of charge carriers, which is explained in Sec. VII.

VII. CONDUCTION MECHANISM

To understand the conduction mechanism of these double perovskites, it is important to get insight into behavior of the charge carriers in the material. In degenerate semiconductors, charge carriers are free to roam. On the contrary, in these types of oxides, charge carriers interact with various inhomogeneities resulting in formation of polarons that have effective mass greater than that of the free charge carriers [44,45]. Furthermore, charge carriers are more or less localized around a particular site due to insufficiency of energy to overcome the barriers. This makes the movement of carrier rather difficult
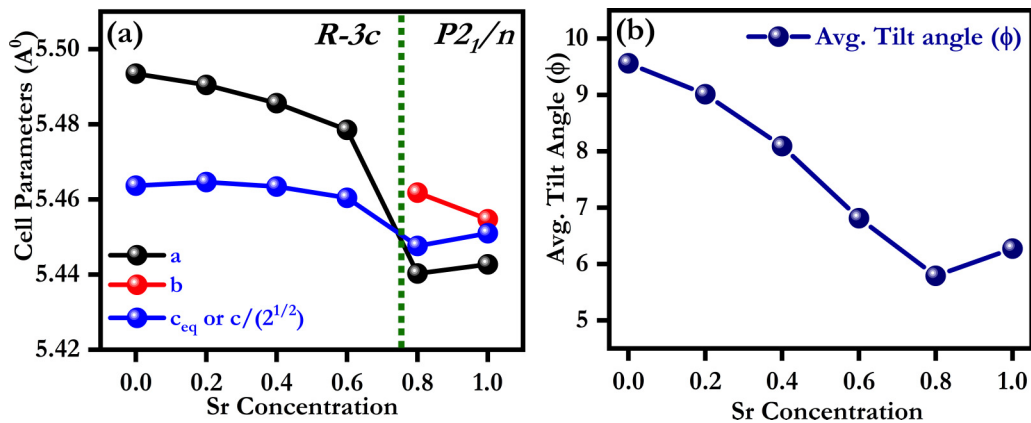
FIG. 6. (a) Change in cell parameters with Sr concentration; For the comparison, we have plotted c_{eq} in the case of R-3c, calculated by $18c_{eq}^2 = c_H^2 + 12a_H^2$ and $c/\sqrt{2}$ in the case of $P2_1/n$ (where c_H and a_H are lattice parameters of the rhombohedral phase in hexagonal setting) and (b) variation of average tilt angle (φ) with Sr concentration.
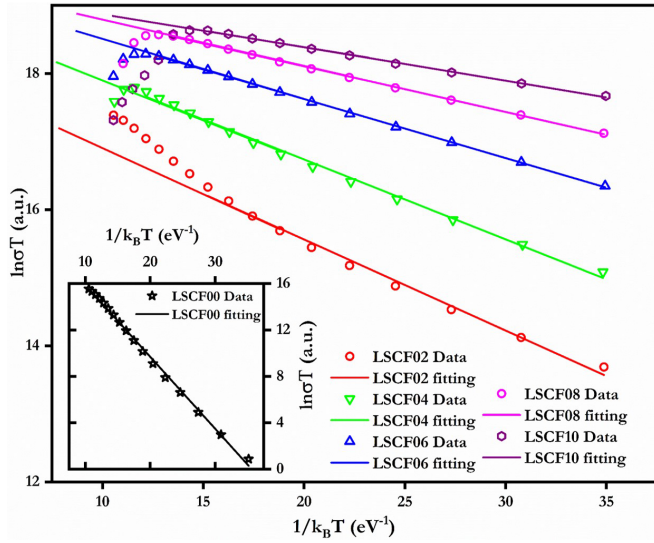
FIG. 7. $\ln \sigma T$ vs $1/k_B T$ plots and fitting with the SPH model for LSCF00 (inset), LSCF02, LSCF04, LSCF 06, LSCF08, and LSCF10 compositions.

as compared to that in degenerate semiconductors. Therefore the small polaron hopping conduction (SPH) model is used to elucidate the conduction mechanisms in these complex oxides [46–48]. The SPH conduction model is expressed by

$$\sigma = \frac{\sigma_o}{T} \exp\left(-\frac{E_{HOP}}{k_B T}\right), \tag{3}$$

where σ represents electrical conductivity, T is temperature in Kelvin, k_B is Boltzmann's constant, σ_o is a constant, and E_{HOP} represents the activation energy for small polaron hopping.

Figure 7 shows the linear fitting of the observed data with the SPH conduction model for all the LSCF compositions. Activation energies for the charge carriers to overcome these energy barriers in these double perovskites were calculated using the slope of the linear fit with Eq. (1) and are included in Table IV. The activation energy for SPH was found to be 0.62 eV for the LSCF00 composition. However, the activation energy decreases sharply with increasing Sr concentration reaching to its more than 12 times lowered value, 0.05 eV, in the composition LSCF10, suggesting that localized holes behave like itinerant ones due to Sr doping in LSCF. This low activation energy corroborates well with the decrease of distortions in octahedra leading towards octahedral ordering, as explained in Sec. VI.

Additionally, to investigate the electrical conductivity in these complex perovskites one has to consider defect chemistry of these materials [49]. As explained by the XPS analysis in Sec. IV, these oxides exhibit multiple oxidation states, which could alter their conduction behavior. It is also important to notice that the Seebeck coefficient exhibits positive values throughout the measurement range, which posits that holes are dominant charge carriers in these oxides. The average oxidation state of Fe and Co, calculated based on XPS results, in LSCF00 is $\sim +3$ and $\sim +2.5$, respectively. These cations occupy the B-site with formal valence of $+4$ in $A_2^{2+}B^{4+}B'^{4+}O_6$ double perovskites resulting into electron-deficient lattice, which is expected to be compensated partly by occupation of La^{3+} at the A site with a formal valence of $+2$, except the holes generated by the $+2.5$ (<3) oxidation state of Co. However, the concentration of holes in LSCF00, would be small and remain localized due to structural distortion induced by octahedral tilting, rendering the low electrical conductivity observed in this compound. In contrast, in the compositions $x \geqslant 0.1$, the situation is quite complex where the A site and B site are in competition with reference to charge accommodation. With increasing Sr content, B-site cations preferred to possess higher oxidation states, as observed in XPS analysis, which is expected to satisfy the charge neutrality condition due to substitution of Sr^{2+} in place of La^{3+} in the A site. As a result, the ratios of Co^{3+}/Co^{2+} and Fe^{4+}/Fe^{3+} were found to be gradually increased with increasing Sr content as evident in our XPS analysis above. This is very important in the perspective of polaron formation, which was found to be the way of charge transport in LSCF compounds as discussed above.

To further gain the comprehension on high electrical conductivity, it is essential to scrutinize effective charge carriers' concentration in the material. The Seebeck coefficient, which is interpreted as an entropy of charge carriers, can be informative. In these types of complex perovskites, the Seebeck coefficient is mostly driven by a hopping conduction of the polaron, given by the SPH model [50,51]. The relation between the Seebeck coefficient and carrier concentration is often expressed by the formula of Heikes [52] modified by Chaikin and Beni [53] as follows:

$$S = \frac{k_B}{e} \ln\left(\frac{2-c}{c}\right), \tag{4}$$

where S is the thermopower/Seebeck coefficient, c is the fractional polaron concentration, e is electronic charge, and

TABLE IV. Fractional polaron concentration and activation energy for SPH conduction model for all the compositions

Composition	Fractional polaron concentration (c) at 323 K	Activation energy for SPH (E_{HOP}) (eV)	E_a (eV) estimated from thermopower data	E_μ ($E_{HOP} - E_a$) (eV)
LSCF00	0.069	0.62	0.083	0.537
LSCF02	0.141	0.13	0.044	0.086
LSCF04	0.409	0.12	0.037	0.083
LSCF06	0.718	0.09	0.021	0.069
LSCF08	0.887	0.07	0.009	0.061
LSCF10	0.999	0.05	0.002	0.048
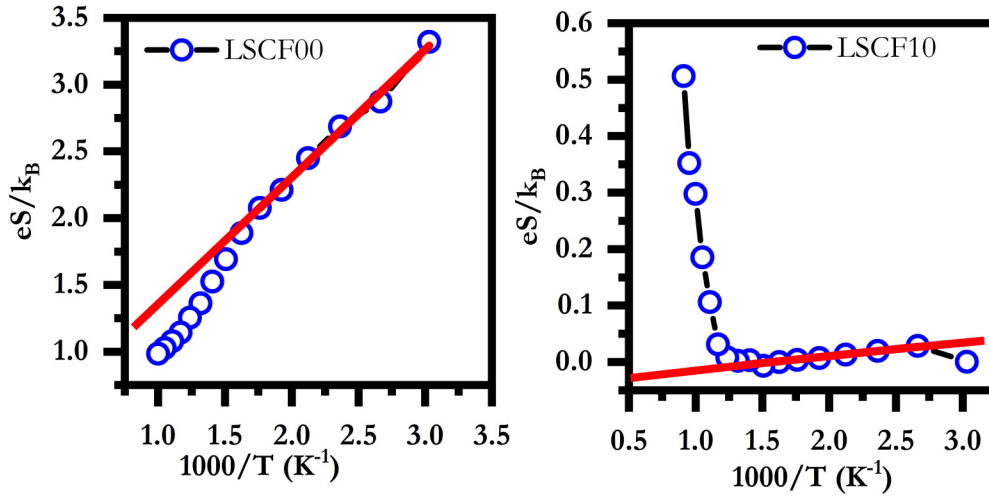
FIG. 8. (eS/k_B) vs $1000/T$ plot and linear fitting for LSCF00 and LSCF10 compositions

k_B is Boltzmann's constant. The modified Heikes formula has been found to be widely used in the literature [50,51,54–56] for explaining the temperature-independent Seebeck coefficient when charge transport is governed by SPH. The calculated values of fractional polaron concentration for LSCF compositions are given in Table IV. It can be inferred from Table IV that LSCF00 contains an almost negligible fraction of polarons, which explains the extremely low electrical conductivity. However, as dopant concentration was increased, a substantial increment in polaron concentration was observed, which correlates well with our XPS analysis demonstrating an increased ratio of Co^{3+}/Co^{2+} and Fe^{4+}/Fe^{3+} cations with increasing Sr content.

Temperature dependent thermopower (S) is further elucidated using the p-type nondegenerate semiconductor model expressed by following equation [46,57]:

$$S = \left(\frac{k_B}{e}\right)\left[\frac{E_a}{k_B T} + A\right], \tag{5}$$

where E_a is the activation energy, A is the constant, and k_B is Boltzmann's constant.

In the SPH transport mechanism, the activation energy can be thought of a contribution due to (a) activation energy associated with charge carrier generation (E_a) and, (b) activation energy for mobility (E_μ); i.e., $E_{HOP} = E_a + E_\mu$. The activation energy for charge carrier generation (E_a) is estimated from the slope of the linear fitting of (eS/k_B) vs $1/T$ as shown in Fig. 8. Activation energy for mobility (E_μ) can be estimated by deducting E_a from E_{HOP}. From Table IV, representing values of E_a, E_{HOP}, and E_μ, it is important to notice that activation energy for charge carrier generation (E_a) is very low as compared to mobility activation energy (E_μ). Much higher activation energy for mobility (E_μ) causing the low mobility of charge carriers suggests the presence of phonon-drag and local disorder in the structure. This kind of dominance of mobility term (E_μ) in activation energy for conduction is typically observed when the charge transport mechanism is governed by SPH [50,58]. It is evident from Table IV that the activation energy for both carrier generation as well as mobility decreases with increase in Sr content. The values of E_a are especially much lower for $x = 0.8$

and 1.0 compositions compared to that for lower Sr content ($0 \leqslant x \leqslant 0.6$) LSCF compositions probably due to the change in crystal structure from rhombohedral to monoclinic symmetry.

So, it can be concluded that Sr doping in LCF double perovskite facilitates the increase in octahedral ordering due to change in crystal symmetry, resulting in a significant increase in fractional polaron concentration, coupled with large reduction in the activation energy barrier for SPH. As a result, the behavior of the charge carrier probably changed from a highly localized state in LCF to itinerant-like charge carriers in highly Sr-doped LCF, causing a manifold increase ($\sim 10^7$ times) in electrical conductivity (σ) and the enhanced thermoelectric power factor of LSCF double perovskites.

VIII. CONCLUSIONS

In summary, a series of compositions of $La_{2-x}Sr_xCoFeO_6$ double perovskite ($x = 0.0, 0.1, 0.2, 0.4, 0.6, 0.8,$ and 1.0) were synthesized via the citrate-nitrate autocombustion route. A single-phase solid solution was confirmed in all the compositions using the XRD technique. Microstructural analysis showed that the grain size increases slightly with increasing Sr concentration. XPS analysis confirmed that Fe and Co tend to show higher oxidation states with increasing Sr content. From the thermoelectric measurements it was observed that the electrical conductivity at room temperature increased more than 10^7 times in LSCF10 as compared to LSCF00. The maximum power factor, $222\,\mu W/mK^2$ was observed in the composition LSCF02. Low thermal conductivity, $1.36\,W/mK$ at 323 K, was found in the composition LSCF02. Best thermoelectric performance, ZT = 0.11, was found in the composition LSCF02. Rietveld refinement of XRD data confirmed that the compositions up to $x \leqslant 0.6$ stabilized in the disordered double perovskite state (R-$3c$ space group), while the compositions, $0.8 \leqslant x \leqslant 1.0$, stabilized in the rock-salt-ordered double perovskite state ($P2_1/n$ space group). The average octahedral tilt angle (φ) was found to be decreased with increasing Sr content, stimulating change in the crystal structure. Octahedral ordering induced liberation of charge carriers (restrained by local fields in these double

perovskites) via significant reduction in the hopping activation energy (E_{HOP}). This was coupled with higher polaron concentration, which is attributed to be the reason behind the manifold increase in electrical conductivity with the increase in Sr content in LSCF double perovskites. Moreover, our current study shows that by manipulating the octahedral tilting, one can design high-temperature high ZT oxides by increasing electrical conductivity in insulator-like double perovskites without compromising other thermoelectric parameters.

[1] D. M. Rowe, *Thermoelectrics Handbook: Macro to Nano* (CRC/Taylor and Francis, London, 2006).

[2] G. J. Snyder and E. S. Toberer, Nat. Mater. **7**, 105 (2008).

[3] P. K. Dager, L. V. Mogni, S. Soria, and A. Caneiro, Ceram. Int. **44**, 2539 (2018).

[4] L. E. Bell, Science **321**, 1457 (2008).

[5] P. Vaqueiro, A. V. Powell, Z. Su, N. Gothard, T. M. Tritt, G. J. Snyder, J. Taftø, M. G. Kanatzidis, M. G. Kanatzidis, D. Vashaee, X. Chen, J. Liu, M. S. Dresselhaus, G. Chen, and Z. Ren, J. Mater. Chem. **20**, 9577 (2010).

[6] S. Walia, R. Weber, K. Latham, P. Petersen, J. T. Abrahamson, M. S. Strano, and K. Kalantar-Zadeh, Adv. Funct. Mater. **21**, 2072 (2011).

[7] S. Walia, R. Weber, S. Sriram, M. Bhaskaran, K. Latham, S. Zhuiykov, and K. Kalantar-zadeh, Energy Environ. Sci. **4**, 3558 (2011).

[8] Y. Pei, J. Lensch-Falk, E. S. Toberer, D. L. Medlin, and G. J. Snyder, Adv. Funct. Mater. **21**, 241 (2011).

[9] T. Okuda, K. Nakanishi, S. Miyasaka, and Y. Tokura, Phys. Rev. B **63**, 113104 (2001).

[10] M. Ohtaki, T. Tsubota, K. Eguchi, and H. Arai, J. Appl. Phys. **79**, 1816 (1996).

[11] M. Molinari, D. A. Tompsett, S. C. Parker, F. Azough, and R. Freer, J. Mater. Chem. A **2**, 14109 (2014).

[12] I. Terasaki, Y. Sasago, and K. Uchinokura, Phys. Rev. B **56**, R12685 (1997).

[13] S. Li, R. Funahashi, I. Matsubara, K. Ueno, S. Sodeoka, and H. Yamada, Chem. Mater. **12**, 2424 (2000).

[14] G. S. Nolas, J. Sharp, and H. J. Goldsmid, *Thermoelectrics* (Springer, Berlin, 2001).

[15] K. Tanwar, M. Saxena, and T. Maiti, J. Appl. Phys. **122**, 164902 (2017).

[16] M. Saxena, P. Roy, M. Acharya, I. Bose, K. Tanwar, and T. Maiti, Appl. Phys. Lett. **109**, 263903 (2016).

[17] P. Roy, V. Waghmare, and T. Maiti, RSC Adv. **6**, 54636 (2016).

[18] S. Vasala and M. Karppinen, Prog. Solid State Chem. **43**, 1 (2015).

[19] R. Pradheesh, H. S. Nair, V. Sankaranarayanan, and K. Sethupathi, Eur. Phys. J. B **85**, 260 (2012).

[20] H. Labrim, A. Jabar, A. Belhaj, S. Ziti, L. Bahmad, L. Laânab, and A. Benyoussef, J. Alloys Compd. **641**, 37 (2015).

[21] G. King, S. Thimmaiah, A. Dwivedi, and P. M. Woodward, Chem. Mater. **19**, 6451 (2007).

[22] P. S. R. Murthy, K. R. Priolkar, P. A. Bhobe, A. Das, P. R. Sarode, and A. K. Nigam, J. Magn. Magn. Mater. **322**, 3704 (2010).

[23] M. T. Anderson, K. B. Greenwood, G. A. Taylor, and K. R. Poeppelmeier, Prog. Solid State Chem. **22**, 197 (1993).

[24] G. A. Slack, *Thermoelectrics Handbook, Macro to Nano*, edited by D. M. Rowe (CRC Press, Boca Raton, 2005).

[25] Z. Chen, X. Zhang, and Y. Pei, Adv. Mater. **30**, 1705617 (2018).

[26] D. Stoeffler and S. Colis, J. Phys.: Condens. Matter **17**, 6415 (2005).

[27] H.-R. Fuh, K.-C. Weng, C.-R. Chang, and Y.-K. Wang, J. Appl. Phys. **117**, 17B902 (2015).

[28] R. Pradheesh, H. S. Nair, V. Sankaranarayanan, and K. Sethupathi, Appl. Phys. Lett. **101**, 142401 (2012).

[29] K. Tanwar, D. S. Gyan, P. Gupta, S. Pandey, O. Parkash, and D. Kumar, RSC Adv. **8**, 19600 (2018).

[30] R. Pradheesh, H. S. Nair, G. R. Haripriya, A. Senyshyn, T. Chatterji, V. Sankaranarayanan, and K. Sethupathi, J. Phys.: Condens. Matter **29**, 095801 (2017).

[31] W. Jones and N. H. March, *Theoretical Solid State Physics* (Dover, NY, 1985).

[32] I. Palchan, M. Crespin, H. Estrade-Szwarckopf, and B. Rousseau, Chem. Phys. Lett. **157**, 321 (1989).

[33] M. C. Biesinger, B. P. Payne, A. P. Grosvenor, L. W. M. Lau, A. R. Gerson, and R. S. C. Smart, Appl. Surf. Sci. **257**, 2717 (2011).

[34] G. Xiao, Q. Liu, S. Wang, V. G. Komvokis, M. D. Amiridis, A. Heyden, S. Ma, and F. Chen, J. Power Sources **202**, 63 (2012).

[35] T. Yamashita and P. Hayes, Appl. Surf. Sci. **254**, 2441 (2008).

[36] K. Zhao, Y. Shen, Z. Huang, F. He, G. Wei, A. Zheng, H. Li, and Z. Zhao, J. Energy Chem. **26**, 501 (2017).

[37] H.-S. Kim, Z. M. Gibbs, Y. Tang, H. Wang, and G. J. Snyder, APL Mater. **3**, 041506 (2015).

[38] J. B. Goodenough, Prog. Solid State Chem. **5**, 145 (1971).

[39] N. Wang, H. Chen, H. He, W. Norimatsu, M. Kusunoki, and K. Koumoto, Sci. Rep. **3**, 3449 (2013).

[40] J. Rodríguez-Carvajal, J. Phys.: Condens. Matter **192**, 55 (1993).

[41] T. Chatterji, B. Ouladdiaf, P. Mandal, B. Bandyopadhyay, and B. Ghosh, Phys. Rev. B **66**, 054403 (2002).

[42] J. Rodríguez-Carvajal, M. Hennion, F. Moussa, A. H. Moudden, L. Pinsard, and A. Revcolevschi, Phys. Rev. B **57**, R3189 (1998).

[43] M. O'Keeffe and B. G. Hyde, Acta Crystallogr. B **33**, 3802 (1977).

[44] F. Bridges, L. Downward, J. J. Neumeier, and T. A. Tyson, Phys. Rev. B **81**, 184401 (2010).

[45] S. J. L. Billinge, R. G. DiFrancesco, G. H. Kwei, J. J. Neumeier, and J. D. Thompson, Phys. Rev. Lett. **77**, 715 (1996).

[46] P. A. Cox, *Transition Metal Oxides: An Introduction to Their Electronic Structure and Properties* (Clarendon, Oxford, 1992).

[47] E. Gorham-Bergeron and D. Emin, Phys. Rev. B **15**, 3667 (1977).

[48] D. Emin, Phys. Rev. Lett. **32**, 303 (1974).

[49] F. A. Kröger and H. J. Vink, Solid State Phys. **3**, 307 (1956).

[50] S. Lee, R. H. T. Wilke, S. Trolier-McKinstry, S. Zhang, and C. A. Randall, Appl. Phys. Lett. **96**, 031910 (2010).

[51] S. Lee, G. Yang, R. H. T. Wilke, S. Trolier-McKinstry, and C. A. Randall, Phys. Rev. B **79**, 134110 (2009).

[52] R. W. U. Heikes, *Thermoelectricity: Science and Engineering* (Interscience Publishers, 1961).

[53] P. M. Chaikin and G. Beni, Phys. Rev. B **13**, 647 (1976).

[54] R. Mahendiran, S. K. Tiwary, A. K. Raychaudhuri, T. V. Ramakrishnan, R. Mahesh, N. Rangavittal, and C. N. R. Rao, Phys. Rev. B **53**, 3348 (1996).

[55] T. Mori, H. Inokuchi, A. Kobayashi, R. Kato, and H. Kobayashi, Phys. Rev. B **38**, 5913 (1988).

[56] P. K. Davies, J. A. Stuart, D. White, C. Lee, P. M. Chaikin, M. J. Naughton, R. C. Yu, and R. L. Ehrenkaufer, Solid State Commun. **64**, 1441 (1987).

[57] N. W. Ashcroft and N. D. Mermin, *Solid State Physics* (Saunders college, Philadelphia, PA, 1976).

[58] T. Holstein, Ann. Phys. (NY) **8**, 343 (1959).